Extending Acoustic Microscopy for Comprehensive Failure Analysis Applications

Sebastian Brand[1], Peter Czurratis[2], Peter Hoffrogge[2], Matthias Petzold[1]

1) *Fraunhofer Institute for Mechanics of Materials IWM, Halle, Germany*
2) *PVA TePla Analytical Systems GmbH, Aalen, Germany*

Sebastian Brand, Ph.D.

Fraunhofer Institute for Mechanics of Materials, IWM

Walter-Huelse-Str. 01

06120 Halle (Saale)

Germany

+49 345 5589 193

+49 345 5589 101

Sebastian.Brand@iwmh.fraunhofer.de

www.iwmh.fraunhofer.de

Abstract

In industrial manufacturing of microelectronic components, non-destructive failure analysis methods are required for either quality control or for providing a rapid fault isolation and defect localization prior to detailed investigations that require a target preparation. Scanning acoustic microscopy (SAM) is a powerful tool enabling the inspection of internal structures in optically opaque materials non-destructively. In addition, depth specific information can be employed for two- and three-dimensional internal imaging without the need of time consuming tomographic scan procedures. The resolution achievable by acoustic microscopy is depending on parameters of both the test equipment and the sample under investigation. However, if applying acoustic microscopy for pure intensity imaging most of its potential remains unused. The aim of the current work was the development of comprehensive analysis algorithms for extending the application of SAM by employing its full potential. Thus, typical case examples representing different fields of application were considered ranging from high density interconnect flip-chip devices over wafer-bonded components to solder tape connectors of a photovoltaic (PV) solar panel and highly integrated chip-to-chip interconnects for 3D integration. The progress achieved during this work can be split into four categories: Signal Analysis and Parametric Imaging (SA-PI), Signal Analysis and Defect Evaluation (SA-DE), Image Processing and Resolution Enhancement (IP-RE) and finally acoustic GHz microscopy for high resolution imaging of dense integrated chip-to-chip interconnections (GHz-SAM). For the first 3 categories data acquisition was performed using a commercially available scanning acoustic microscope equipped with several ultrasonic transducers covering the frequency range from 15 MHz to 175 MHz. In the fourth example data acquisition was performed using the prototype ad a novel acoustic GHz microscopy tool which is currently under development into a commercial system. The acoustic data recorded were subjected to sophisticated algorithms operating in time-, frequency- and spatial domain for performing signal- and image analysis. In all four of the presented applications acoustic microscopy combined with signal- and image processing algorithms proved to be a powerful tool for non-destructive inspection.

keywords: quantitative acoustic microscopy, acoustic parametric imaging, automated defect localization, acoustic GHz-microscopy, micro bump, high resolution delamination analysis

Parts of the work contained in this publication has originally been presented at the 37th International Symposium for Testing and Failure Analysis 2010 in Dallas, TX.

Introduction

Inspection methods operating non-destructively are required in many applications in the field of failure analysis including quality control and fault localization prior to destructive target preparation for detailed micro-structural investigations. Providing the option of running multiple tests on the same sample methods operating non-destructively also extends the level of investigation and thus, the understanding of the defect formation, failures and their root causes. However, non-destructivity is always connected with a trade-off between comprehensive destructive preparations and resolution. Scanning acoustic microscopy employing ultrasonic signals ranging from the MHz- up to the GHz- frequency band allow resolutions from the mm- down to the µm range. The final resolution achievable however, is depending on various parameters namely the acoustic frequency, the transducers aperture but also the sound velocity and the acoustic attenuation of the material and the depth of the structure under investigation. While the aperture of the inspection transducer can be tailored for specific applications wave attenuation is inevitably proportional to frequency and the materials acoustic attenuation [1]. In acoustics, attenuation covers several phenomena which contribute to a decrease of the amplitude of the acoustic wave and its spectral content. Major attenuation effects are caused by absorption and scattering, but also structural and chemical relaxation processes lead to a decrease in acoustic intensity. For increasing the penetration depth, the acoustic frequency has to be lowered which is, however, related to a decreased lateral resolution. The interaction of acoustic waves with matter is characterized by phenomena like reflection, diffraction and scattering caused by structural, size and mechanical properties of the sample and its microscopic sub-structure. Therefore, echo signals received from a sample contain characteristic information on the samples properties. By employing appropriate signal analysis algorithms to time domain echo signals acquired by the acoustic microscope, parameters related to structural and mechanical properties of the inspected sample can be derived. Thus, by analyzing the echo signals comprehensive information on the samples condition and composition can be obtained. In situations were acoustic microscopy is applied for pure qualitative imaging of internal structures, like delaminated spots in a bonding interface, additional image processing and analysis can improve resolution and contrast for

revealing and emphasizing various defects even in an early state of its propagation.

The current work is focused on the development of comprehensive analysis tools for extending acoustic microscopy by signal and image processing algorithms, enabling a broad range of applications in the field of failure analysis. In this paper four case studies representing different fields of application are described targeting developments in parametric imaging, defect evaluation, image processing and acoustic GHz-microscopy. Signal analysis and parametric imaging is applied for estimating the adhesive condition of a solder tape of a PV-solar panel. The flip-chip contacts of a CPU-device were evaluated and classified employing extended signal analysis. Delaminated regions in wafer-bonded interfaces were inspected and images have been processed for increasing the resolution and the contrast. Finally, acoustic GHz-microscopy was applied for localizing delaminations in highly integrated chip-to-chip interconnects relevant for 3D-integration processes. In all four applications the acoustically obtained results were improved and additional information on the defect situation have been provided.

Material and Methods

Data Acquisition

In three of the four examples presented here acoustic data acquisition was performed using a fast scanning acoustic microscope (Evolution II, PVA Tepla Analytical Systems GmbH, Aalen, Germany) equipped with several transducers covering a frequency range from 15 MHz up to 175 MHz. The focal length of the transducers also differed from 5.9 mm @ 175 MHz up to 20 mm @ 15 MHz. Echo signals were digitized with a sampling rate of 500 MS/s at a resolution of 8 bit. The unprocessed digital rf-signals were stored on the microscopes internal hard drive for further off-line analyses. During scanning, the samples were submerged in de-ionized and degassed water which acted as the coupling medium for the acoustic wave propagation. Data analysis and image reconstruction was performed using the MATLAB based acoustic analysis software SAMNALYSIS, developed at the Fraunhofer Institute for Mechanics of Materials, IWM, Halle,

Germany. Acoustic GHz-microscopy was performed using a custom-made set-up which is currently under development into a commercial system.

Signal Processing

Signal processing algorithms and data reconstruction was developed using MATLAB (The Mathworks, Natick, USA). The algorithms developed during this work were combined into the SAMNALYSIS toolbox that can be applied for performing comprehensive and complex analyses on acoustic data and images. The entire software was compiled using the MATLAB compiler and thus, can be run on any Microsoft Windows based computer for off-line analysis of recorded rf-ultrasonic signals.

Signal Analysis and Parametric Imaging (SA-PI)

For illustrating the application of parametric imaging in combination with signal analysis photovoltaic (PV) solar cells as shown by the schematic in figure 1 have been employed. The samples consisted of polycrystalline silicon wafers with a thickness of 220 µm. For electrical connectivity, a tinned copper interconnect ribbon of 100 µm thickness and 5 mm width was soldered on top of the solar cell's bus bar. The solder had a thickness of approx. 30 µm on each side of the tape. The acoustic inspection was performed as described above. For optimizing the acoustic images using appropriate processing and analysis algorithms, the echo signals were subjected to a cepstral analysis [2]. Parametric imaging allows the visualization of parameter changes caused by specific defects related to characteristic sample properties. The example shown here employs the transformation of the time domain signals into the cepstral domain. In the cepstral-domain, features representing the periodicity of the spectra can be derived which are related to the temporal and thus, the spatial separation between echo pulses in the time domain signal. By employing the corresponding value of the sound velocity, the physical separation between interfaces can be estimated. The main advantage of transferring the acoustic data into the cepstral domain is the ability to estimate pulse separations even when pulses overlap. In locations where the solder tape is delaminated from the bus bar of the PV-panel, a strong reflectivity occurs at the interface tape-coupling fluid, resulting not only in a

strong echo at this interface but also in the occurrence of multiple reflections which can be observed as reverberations in the received acoustic signal. When inspecting a well soldered region, the acoustic signal obtained is expected to contain echo pulses at the tape/bus-bar interface with a lower amplitude that is caused by the lower reflectivity and the higher transmission coefficient of the properly soldered interface. The signal obtained here is also expected to lack a strong reverberation, resulting in a low number of reoccurring echo pulses.

From the cepstra computed using the time domain signals, the position index of the first maximum was extracted. The parametric imaging was then performed by color coding of the parameter values and mapping as a two dimensional image.

It should be noted that parametric imaging can be performed using any relevant parameter of the underlying acoustic signal representing a signal property related to the defect of interest. For verifying the findings obtained by acoustic microscopy and subsequent signal analysis complementary x-ray inspection was conducted using a NANOMEX 180nf CT (Phoenix x-ray, Wunstorf, Germany).

Signal Analysis and Defect Evaluation (SA-DE)

CPU devices manufactured in flip-chip technology were investigated for evaluating and classifying the conditions of the solder bump contacts using acoustic microscopy at 175 MHz acoustic frequency. The samples used are illustrated in figure 2. The flip-chip contacts connected the 750 µm thick silicon die with the organic laminate substrate of the CPU device. The solder bumps had a lateral diameter of 80 µm and the die size of the flip-chip was 20 mm by 30 mm. To support the reliability behavior and the mechanical stability, a polymeric underfiller was contained between the organic laminate and the silicon die.

Signal Analysis and Defect Classification:

The lateral locations of the flip-chip contacts were estimated by differentiating between the interfaces silicon/solder-contact and silicon/underfill using characteristic reflective features of the interfaces as illustrated in figure 3. Figure 3-right shows the Hilbert transformed acoustic cross section of a CPU-sample used here. Echoes occurring at the silicon/solder-contact interface were considerably longer than echoes from the silicon/underfill interface. Parameter

values of the backscatter amplitude integral (BAI) were computed within the time range between the exit echo of the silicon and the signal peak at the solder/substrate interface as indicated by the red rectangle in the acoustic cross-section in figure 3. Further analyses have been applied to signals of the solder interconnections exclusively for characterization of the contact condition. These processing steps included wavelet analysis employing a Gaussian mother wavelet of the 4th order for deriving wavelet coefficients versus scaling factors and time. Wavelet analysis is a 2-D redundant signal transformation which overcomes the main weaknesses of the short-time-Fourier-transformation (STFT). The application of a static window length as used in STFT results in a constant time and frequency resolution of the transformed signal. In wavelet analysis, the analyzing wavelet is expanded and compressed in addition to sliding over the signal analyzed. This adaptation results in an improved temporal and spectral resolution, which cannot be obtained by a Fourier transformation [5]. During scaling of the analyzing wavelet, the number of oscillations of the wavelet remains constant, resulting in a variation of the spectral content. Wavelet analysis of a signal computes coefficients at different scaling factors describing the correspondence between the analyzing wavelet and the signal. For illustration, a wavelet coefficient corresponds to the area below the result of the multiplication of the analyzing wavelet and the signal at a particular wavelet scaling. Although the STFT provides a complex coefficient for one parameter (frequency), the continuous wavelet transform (CWT) computes one coefficient for each combination of the scaling factor and the temporal position. The wavelet transformation performed in the current study used the MATLAB functions for the CWT. The choice of a Gaussian wavelet of the fourth order can be explained by its similarity to the ultrasonic pulses used in the experiments. Wavelet analysis was applied to the signals obtained at positions which were detected to be a flip-chip contact. The distribution (mean and standard deviation) of the wavelet coefficients were computed versus scaling factors and as a function of the temporal position.

In addition to wavelet coefficients, the backscatter amplitude integral (BAI), the relative peak positions, the peak amplitudes and the corresponding pulse widths at the silicon-solder interface were computed. For estimating the pulse width, the peak positions and the peak amplitudes time signals were first transformed into the Hilbert domain and the pulse width was obtained in ns at -6

dB of the peak amplitude. The BAI can be computed according to [3] as the integral of the Hilbert transformed absolute values of the time signal prior to low pass filtering. Due to integration over time, multiple echoes can be included in the BAI computation resulting in an improved contrast. Finally, the parameters of the peak position, the BAI and the wavelet distribution were scaled, thresholded and combined in a classifier for deriving a binary void-intact decision for each pixel recorded at an individual flip-chip contact. To provide an easy-to-handle visual indication the resulting decision matrix was color coded and superimposed to the BAI-parametric image.

Complementary Defect Assessment:

During the method development, locations of defective solder contacts were estimated using x-ray microscopy (XD7600, Dage). From these known void and known intact positions, ultrasonic data were acquired and signal parameters were computed for comparison to parameter values obtained at known intact interconnects. Characteristic parameter ranges of the peak position, pulse length, BAI and the distributions of the wavelet coefficients versus time and temporal positions were estimated from the acoustic data and implemented in the analysis algorithm. Thresholds for the classification were defined for each of the mentioned parameters using half of the Euclidic distance between the mean values of the two categories.

Verification by SEM and X-Ray Microscopy:

For verification of the methods accuracy, the success rate of the acoustic defect estimation was evaluated using “unknown” samples. Void positions were estimated from the ultrasonic data and the binary decision matrix was computed. The results were handed to an experienced technician for verifying the defects using X-ray microscopy. Finally, the two rows containing the highest number of defective contacts were cross-sectioned, polished, and high resolution imaging was performed by scanning electron microscopy (TM1000, Hitachi).

Image Processing and Resolution Enhancement (IP-RE)

The potential of acoustic image processing and resolution enhancement is illustrated by inspecting bonding interfaces between silicon wafers. Acoustic micrographs were recorded at the interface of two bonded wafers. Both wafers had a thickness of 500 µm and were originally prepared and patterned for mechanical strength testing (chevron- and tensile tests). Bonding was based on a plasma-activated low temperature silicon direct wafer bonding process. Prior to the mechanical tests, samples were inspected by acoustic microscopy to investigate the geometric accuracy of the bonded structures, which is of major relevance for the reliability of the mechanical test results. Acoustic micrographs were computed from the rectified and integrated echo signal at the bonding interface. Locations of intact bonding contain a lower reflectivity at the bonding interface compared to delaminated or non-bonded regions. When passing interfaces between materials with differing elastic or mechanical properties, sound waves are partially reflected and transmitted. The degree of reflection strongly depends on the mismatch in acoustic impedance between the neighboring materials. Acoustic impedance is defined as the product of sound velocity and mass density. The case of a delamination containing a gas filled gap represents an extreme mismatch in acoustic impedance resulting in a reflectivity of almost 100 %. Thus, delaminated spots are clearly visible and easy to detect in acoustic micrographs, although the axial dimension of the delamination is much smaller than the wavelength of the acoustic wave. This phenomenon can be considered as the modulation of the surface reflectivity by a thin gaseous layer. Acoustic micrographs were then processed using image processing filters for blind deconvolution [4], a Gaussian filter and a Sobel filter for emphasizing the edges of the bonded structures, enabling the evaluation of the geometric accuracy. Image contrast was adapted manually for matching the gray levels to the dynamic range of the images appropriately.

High resolution Acoustic GHz-Microscopy for the assessment of electrical defects in 3D-integrated devices (GHz-SAM)

The fourth case study presented here applies acoustic GHz-microscopy for localizing adhesion defects in devices relevant for 3D-integration. This

application is of great interest for wafer bonding technologies that, in addition to mechanical 3D assembly, are also often used to form buried electrical chip-to chip interconnects with bonding pitch dimensions on the order of 10 µm. Samples inspected contained high density interconnects (10^6 per cm^2) forming large area arrays (512 x 640) on 10 µm and 15 µm pitch. The devices were thermo-compression bonded using Cu/Sn-Cu interconnects at a temperature of 275 °C and a pressure of 50 MPa. For the 10 µm pitch devices, the bottom die consisted of metal links terminated with 6 µm diameter pads that were plated with 4 µm of Cu and then coated with BCB. The 15 µm pitch devices had the same micro-pillar dimensions as the 10 µm pitch devices. Vias were etched in the BCB to create openings for bonding to the Cu pads. The BCB sidewalls created a mechanical key to prevent lateral slippage during bonding [6]. Acoustic inspection was performed through the BCB mechanical key after removal of the top die.

For data acquisition an acoustic GHz-microscope set-up was used which is currently under development into a commercial system. This set-up employed short tone-bursts, which are narrow band pulses with a bandwidth of approximately 10 %. The center frequency of these bursts was 1 GHz and the pulse length was 20 ns. The scan resolution was set to 390 nm and the scan field had a size of 200 µm by 200 µm. Acoustic inspection was performed using a highly focused acoustic 1 GHz lens (PVA TePla Analytical Systems GmbH, Aalen, Germany). The focal diameter of this acoustic lens is approx. 1 µm in water with a focal distance of approx. 76 µm. For data acquisition several scan planes were recorded at decreasing distances between the transducer and sample under investigation, resulting in a focussing inside the sample. In total 35 scan planes at adjacent scan distances have been acquired. The set-up applied automatically pre-processed the acoustic time domain data using a so called box-car integrator, which estimates the signal envelope and integrates the echoes within a specified time-gate.

Defect verification by FIB target preparation and SEM imaging

For verification target preparation was performed on spots where delaminations have been identified using the acoustic GHz-microscope set-up. Using focused ion beam technology a trench of approx. 80 µm length, 10 µm width and 10 µm

depth has been milled through the BCB layer, the micro-bumps and the substrate. The edge of the trench was then imaged using scanning electron microscopy (SEM). The combined FIB/SEM system used was a V600 (FEI, Hillsboro, USA).

Results and Discussion

Signal Analysis and Parametric Imaging (SA-PI)

The connectivity of a solder tape on top of a solar panel was assessed by computing the position of the first cepstral maximum from time domain signals acquired using acoustic microscopy. The image in figure 5-top shows a regular acoustic micrograph of the solar panel with the solder tape in the vertical center. The contrast in that image arises from the maximum amplitude of the recorded echo signals. In figure 5-bottom the time domain signals are plotted as an acoustic cross-section. The position of the cross section corresponds to the red mark in the acoustic image (figure 5-top). On the left side the solder tape is detached (delaminated) from the bus bar of the solar panel the red-marked line in the acoustic micrograph in figure 5-top. It can be seen that the echo distribution is not homogeneous which causes multiple reflections (reverberations) of the acoustic signal within the tape. By applying a cepstral analysis the echo separation and periodicity was extracted. The parameter matrix containing the position of the first cepstral maximum is plotted in the top-image of figure 6. This parameter map corresponds well to the location of the defect positions that can be derived from figure 5-bottom. In the top-image in figure 6 regions of well adhesion between the tape and the bus-bar can be identified. In locations of adhesion only an entrance and a small exit echo occur, leading to a low position index of the cepstral maximum. In contrast, delaminated areas lead to reverberations, resulting in an increased position index of the cepstral peak and the corresponding amplitude. In this parametric image, complete adhesion is expressed by the blue coding, while increasing values of the cepstral maximum position index are stained yellow to red. For verification of these findings, complementary x-ray microscopy was performed. The image in figure 6-bottom shows the result of the X-ray microscopy. Although delaminations only cause limited absorption contrast in X-ray some, delaminations can be seen. For contrast improvement the x-ray images

were plotted in false-color. The parametric imaging enables a simplified assessment of the solder quality of the contact ribbon. Further thresholding would allow for binary imaging and automated classification.

Signal Analysis and Defect Evaluation (SA-DE)

Acoustic Analysis: interconnect localization

According to the acoustic cross-section contained in the image to the right in figure 3, interconnect positions were located using the pulse length of the echoes obtained at the silicon/solder contact interface. In presence of a flip-chip contact, the peak amplitude of the echo at the silicon-connector interface was 200% higher compared to the signals measured at the interface silicon/underfill. The pulse width obtained from a contact was 30 ns while the echo at the silicon/underfill interface was only 10 ns long. Figure 7 shows two Hilbert transformed signals recorded at the location of a flip-chip interconnect (black) and in between two contacts (silicon/underfill) (red). The differences in the peak amplitudes and pulse widths are evident from the signals plotted in figure 7.

Acoustic Analysis: defect classification

Wavelet analysis was applied to the echo signals recorded at the silicon/interconnect interface. Significant differences in the distributions of the wavelet coefficients were observed between intact and defect flip-chip contacts. Wavelet coefficients estimated from a void showed a broader distribution versus scaling factors and wavelet positions compared to values obtained from an intact contact. In case of a void, wavelet coefficients of equal amplitude occur with a much broader distribution over all wavelet positions. The average distribution width versus the scaling factors (sf) was 1.7 sf for intact connectors and 2.5 sf for the voids. For illustration, figure 8 contains results obtained by wavelet analysis. The wavelet coefficients computed from the ultrasonic signals recorded at an intact flip-chip interconnect are plotted in the left-hand-side image in figure 8, while the right-hand-side image illustrates the wavelet coefficients obtained from a defective interconnect. Distributions were estimated at 70% of the maximum values. Another parameter included in the classification was the relative position

of the signal peak at the silicon/solder interface. Pulse shifts of up to 20 ns between intact and defective contacts were observed. Both parameters were combined in a linear classifier for increasing the success rate and to optimize for false- positive classifications. Figure 9 shows the results estimated by the classifier. Green indicated spots in figure 9-left specify positions of intact solder-connectors. Voids and false-positive contact positions are marked red. The settings and parameter ranges applied for computing the results in figure 9-left were optimized for classification of the flip chip-contacts at the outer rim of the flip-chip device. For classifying the inner interconnects the application of adapted settings will be required to obtain a robust computation and reliable results. The graph on the right-hand-side in figure 9 illustrates the individual parameter values at the interconnect-locations. Parameter values were thresholded, scaled to 255 (8bit) and plotted color specific in this graph. At locations where all parameters reached the threshold defined for an intact connector, the pixel in the image is white, since the values of each color channel is 255. In locations were an intact flip-chip contact has not been identified (since not all parameters reached the level of 255), the pixel values deviate from white. Green indicated are all pixels that have been identified not to be a flip-chip interconnect.

Verification by SEM and X-ray microscopy

For validation of the defect classification based on the acoustic microscopy data both, scanning electron and X-ray microscopy were applied to the same CPU device. The decision map (figure 9-left) generated by the analysis algorithm developed here was given to a technical assistant experienced in void detection using the x-ray microscope. In Figure 9-center all voids detected based on the acoustic microscopy data are indicated by a yellow mark. Red indication in Fig. 9-center corresponds to voids that have been confirmed by X-ray microscopy. It can be seen that 8 out of 31 voids estimated from the acoustic data could not be confirmed by X-ray, although they have been pointed out explicitly by the acoustically based decision map, which was handed to the technician for assisting the X-ray inspection. This leads to an assumption of 25.8 % false-positive classification. However, in addition to X-ray microscopy scanning electron microscopy was applied to the two rows of connectors with the highest number of voids detected acoustically. For acquiring electron micrographs the CPU device

was sequentially polished to the middle of each interconnect row and then further prepared for SEM-imaging. Voids revealed by SEM-imaging are indicated by a white circle in figure 9-center. It can be seen that thirteen voids detected by analyzing the ultrasonic echo signals could be verified by SEM imaging. However, it also shows that two false-positive and one false-negative detections occurred, which corresponds to an overall success rate of 90.3 % including both kinds of false detection. Figure 10 contains electron micrographs of the contacts that could not be verified by x-ray microscopy, but were revealed when analyzing ultrasonic signals obtained by scanning acoustic microscopy. It can be seen that all of the flip-chip-contacts are disconnected from the substrate. The numbering in figure 9-center corresponds to the numbering in figure 10 (top-right corner of each scanning electron micrograph). The electron micrograph in figure 10-1 reveals that this particular interconnect is only partially disconnected and also shows a noticeable thinner gap between the contact and its socket compared to the other voids. This kind of defect will show an electrical connection during electronic testing. However, in a practical application this interconnect will definitely fail due to thermal processes caused by the applied electrical current. It was somewhat surprising to see this kind of void being detected non-destructively using acoustic microscopy inspection. The micrographs 2 – 6 displayed in figure 10 clearly show the flip-chip interconnects to be defective. However, none of these defects has been detected by X-ray microscopy, although they have been pointed out explicitly by the acoustically based decision map (except the interconnect in 10-2, which was a false positive detection of the acoustic analysis).

Image Processing and Resolution Enhancement (IP-RE)

Image processing was applied to acoustic micrographs recorded at the bonding interface of wafer bonded structures. The acoustic micrographs did not show sufficient contrast and sharpness to clearly evaluate defects located at the bonding interface. In figure 11 the acoustic micrographs prior to the image processing are plotted in the upper row. Performed was blind-deconvolution for increasing the sharpness of the images. Additionally, a Sobel filter was applied to the regions of interest (ROI's) in the left and right images in figure 11. A Gaussian filter was applied to the central image in figure 11. The samples shown to the left and right in figure 11 were prepared for chevron testing of the bonding strength while the

sample in the center was prepared for a tensile test. The ideal shapes for performing chevron- and tensile mechanical tests on bonded structures are illustrated in figure 4. Deviations from this structure will lead to a falsification of the strength values and thus of the derived adhesive properties of the tested samples. The application of acoustic microscopy revealed that none of the samples shown here were suitable for mechanical testing, since regions outside the intended structure were also bonded to the substrate, not allowing the estimation of reliable results. However, in all three cases small defects have also been discovered along the edges of the intended bonding structure. The application of the image processing enabled a resolution and contrast enhancement for emphasizing defect sizes and orientations and thus, an evaluation of the samples suitability in a non-destructive test.

High resolution Acoustic GHz-Microscopy for the assessment of electrical defects in 3D-integrated devices (GHz-SAM)

The application of highly focusing ultrasonic transducers at 1 GHz acoustic frequency enabled imaging of the sub-surface structure in micro-bump devices relevant for 3D-integration. Delaminations of the electrical routings from the bonding substrate has been imaged through the polymer (BCB) layer with a lateral resolution below 3 µm. During data acquisition the transducer was defocused towards the sample surface and an acoustic scan has been acquired at each defocus position. Figure 12 shows an acoustic micrograph at approx. -15 µm defocus (towards the sample surface). The electrical routings behind the 5 µm of polymer can clearly be seen. Delaminations between the routings and the bonding substrate appear bright, due to the increased reflectivity at a delaminated interface. An acoustic cross section through the samples top-layer is displayed in the right-hand-side image in figure 12. This image corresponds to the cross section along the red marked line in the acoustic micrograph in the left-hand-side image. The bright vertical lines correspond to delamination defects as verified by SEM imaging. Shown in the top image of figure 13 the is the physical cross-section through the micro-bumps and the polymer BCB layer. The trench was prepared by Focused Ion Beam (FIB) and then imaged by SEM. The bottom image of figure 13 displays the acoustic micrograph with an indication of the trench. In figure 14

the defect region is zoomed in for displaying the details of the delamination. It can clearly be seen that the polymer layer and the electrical routing are detached.

Conclusions

The signal- and image analysis tools developed for improving the performance of acoustic analysis showed positive results. It was possible to extend the application of acoustic microscopy from pure qualitative imaging to parametric imaging and thus, semi-quantitative parameter estimation applicable in a broad range of different fields of applications. Additionally, an automated operating method for defect evaluation of interconnects was developed, based on acoustic microscopy data. Finally, the combination of acoustic imaging with image analysis and processing also proved successful for increasing image detail and contrast. Further image processing filters will be included stepwise into the analysis toolbox in the near future, for extending the optimization of the acoustic micrographs. For the first time acoustic GHz-microscopy was applied to localize delaminations in micro-bump arrays relevant for 3D-integration of microelectronic devices. It enabled imaging through a polymer layer providing a resolution in the 3 μm range. Defects detected have been verified be FIB preparation and SEM imaging. The acoustic GHz-microscope appears to be a valuable tool for defect localization in highly integrated devices.

References

[1] Briggs, A, Advances in Acoustic Microscopy, Plenum Press (New York and London, 1995)

[2] Ziegler, K., "Cepstrum Analysis of Voice disturbances" *Folia Phoniatrica et Logopaedica*", Vol. 47, No. 4 (1995), pp. 210-217.

[3] Raum, K., *et al.,* "Channel defect detection in food packages using integrated backscatter ultrasound imaging", *IEEE Transactions on Ultrasonics Ferroelectrics and Frequency Control*, Vol. 45, No.1 (1998), pp. 30-40.

[4] Cannon, M., "Blind deconvolution of spatially invariant image blurs with phase", *IEEE Transactions on Acoustics, Speech and Signal Processing*, Vol. 24, No. 1 (1976), pp. 58-63.

[5] Graps, A. “An introduction to Wavelets.”, *IEEE Transactions on Comp Sci Eng*, Vol 2, No. 2 (1995), pp. 50-61.

[6] Reed J.D., Lueck M., Gregory C., Huffman A., Lannon J.M. Jr., Temple D.S., “Low Temperature Bonding of High Density Large Area Array Interconnects for 3D Integration”, 43rd IMAPS Conference, Raleigh, NC November 2, 2010.

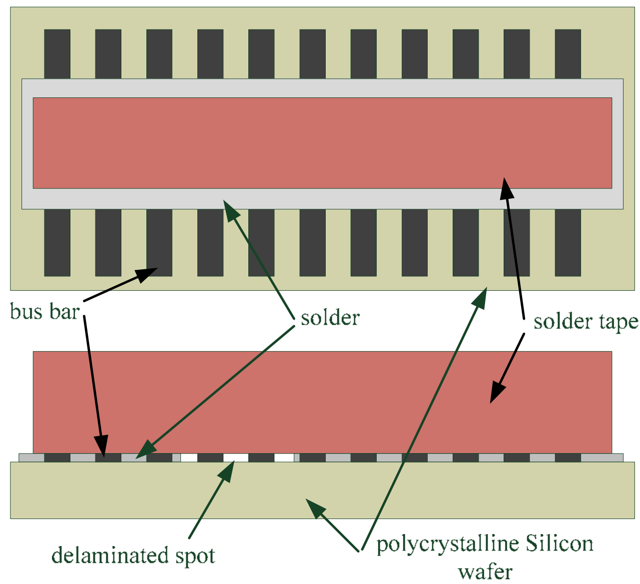

Figure 1: Sample description for signal analysis and parametric imaging. Illustration of a PV-solar cell with bus bar and soldeed Cu ribbon for electrically connecting the bus bar to the external electronics. The cell had a thickness of 220 µm, while the Cu riboon thickness was 1 mm. Approx. 30 µm of solder was contained on top and beneath the ribbon. The ribbon width was 5 mm.

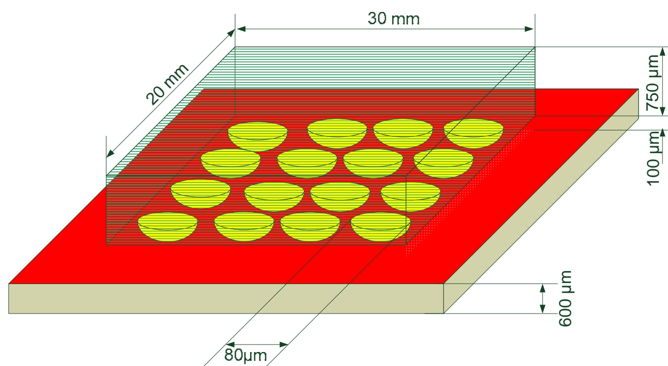

Figure 2: Sample description for signal analysis and defect evaluation. The sample was a CPU device manufactured in flip-chip technology on top of an organic substrate. The dies thickness was 750 µm, with flip-chip contacts of height 100 µm and diameter 80 µm. The lateral dimension of the die was 20 mm by 30 mm. Acoustic inspection was performed through the die after the cap of the CPU was removed.

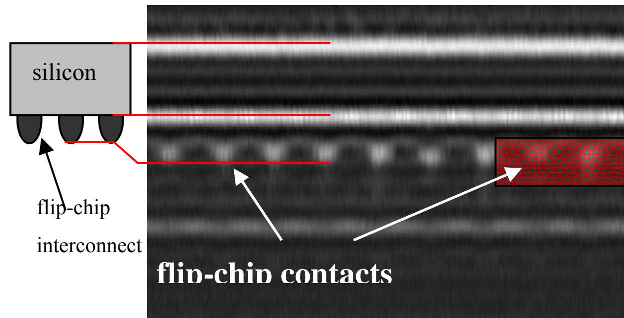

Figure 3: Internal sample structure and echo signal occurrence. The schematic on the left illustrates the 750 µm silicon layer with the flip-chip contacts underneath. On the right, an acoustic cross-section image through the CPU-device is shown. Boundaries and corresponding echoes are indicated by red lines. The red rectangle shows the time range for estimating BAI values.

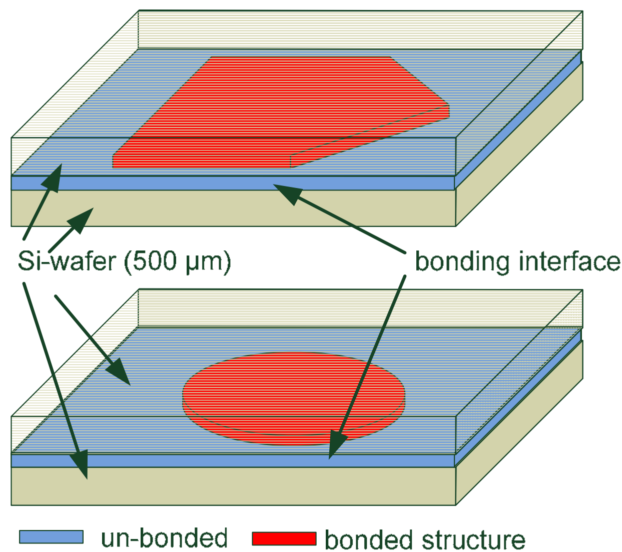

Figure 4: Description of samples used for image processing and resolution enhancement. Samples consisted of patterned and bonded wafers for additional mechanical strength testing. Both wafers had a thickness of 500 µm and surface area of 1 mm by 1 mm. The red indicated area was the bonded structure while the blue indication represents un-bonded interfaces. For mechanical testing, the accuracy of the bonded structure strongly impacts the test reliability.

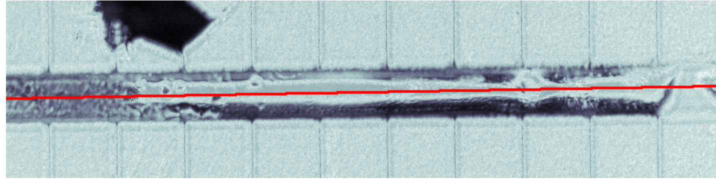

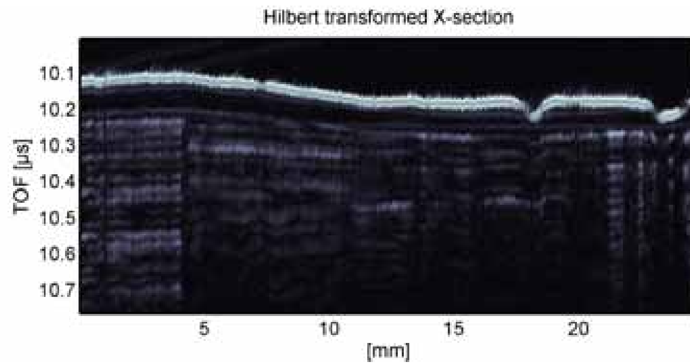

Figure 5: Acoustic inspection of the connective properties of a Cu ribbon soldered on top of a PV solar panel. Top: regular acoustic micrograph representing the maximum amplitude values of the acoustic echo signal. Bottom: Acoustic cross-section along the red marker in the acoustic micrograph (top image). To the left and to the right delaminated areas can be seen from the reverberating echoes.

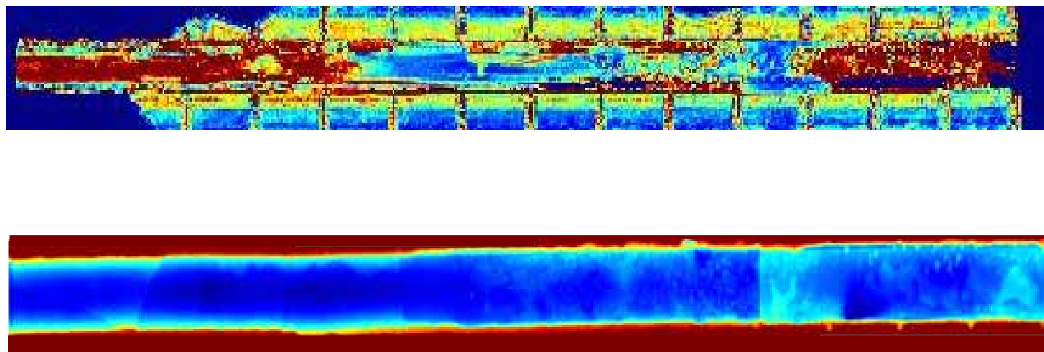

Figure 6: Results of the parametric imaging based on acoustic microscopy. Top: Parametric image displaying the peak position of the cepstrum. Blue regions in the image correspond to intact soldering and thus, good adhesion. Yellow and red pixels indicate disconnected areas. It can be seen that most of the tape is not connected to the bus-bar of the PV-panel. Bottom: Complementary X-Ray micrograph of the same region of the tape. Some delaminations can be seen, although the contrast of is rather poor.

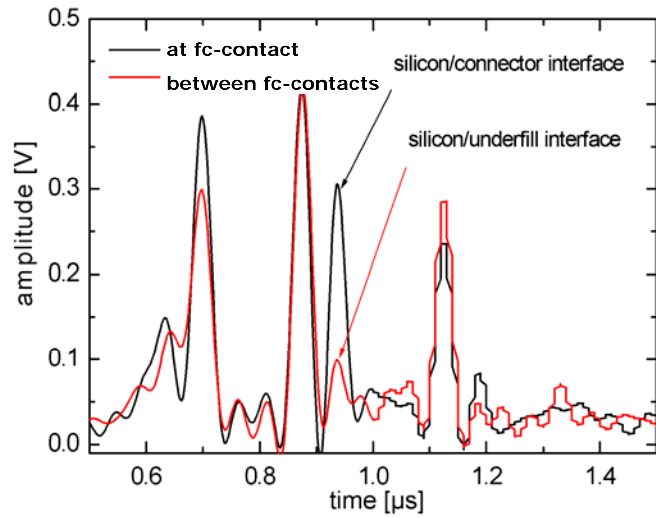

Figure 7: Hilbert transformed and low pass filtered signals. The black and red curves were computed from signals recorded in presence and absence of an interconnect, respectively.

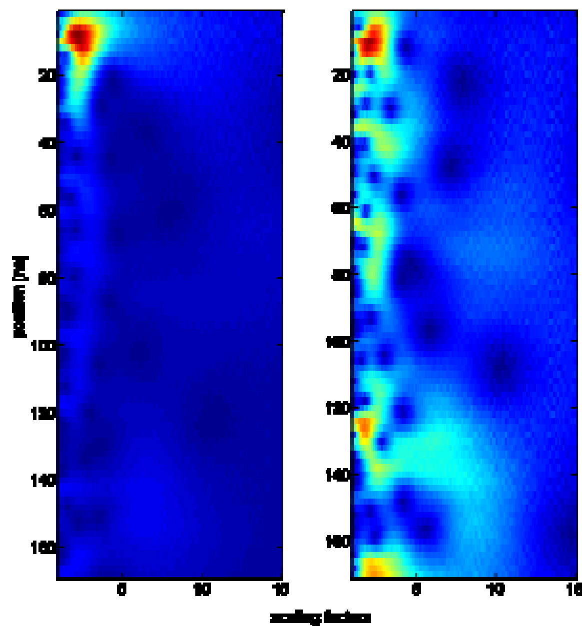

Figure 8: Wavelet coefficients estimated at the silicon/solder interfaces of an intact (left) and at a defect interconnect (right).

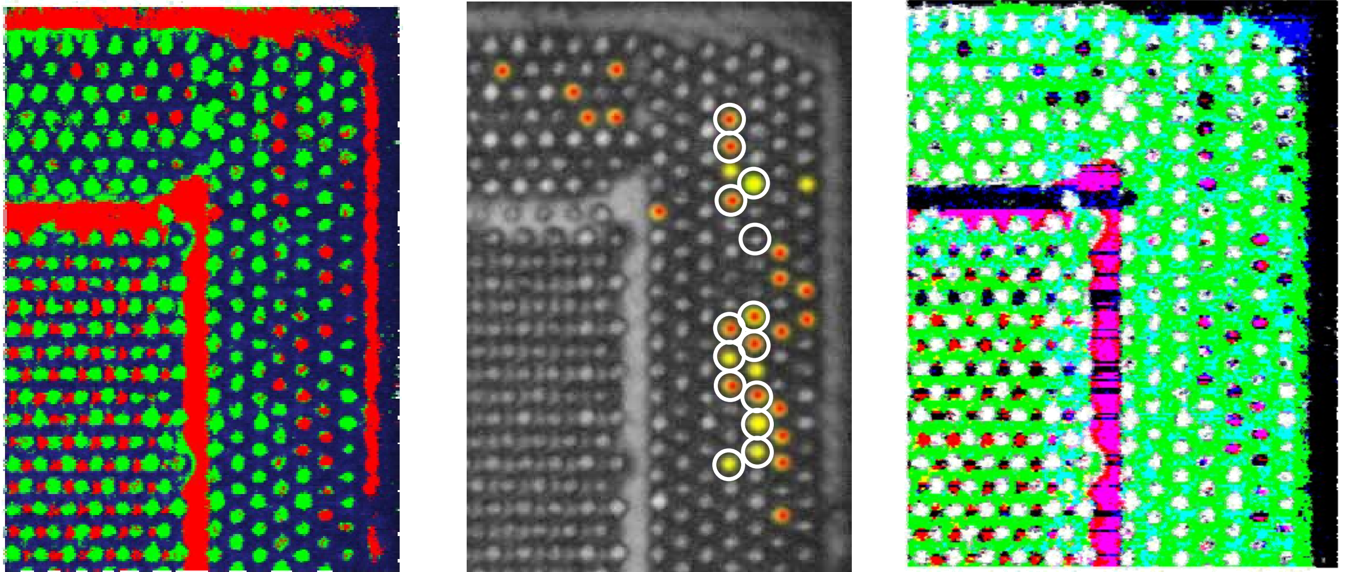

Figure 9: Classification results and evaluation of void detection. LEFT: green indicated are extracted flip-chip contacts. Red interconnects were classified as voids based on the wavelet coefficients and pulse separation characteristics at the interface silicon/ solder. CENTER: BAI-parametric image with indication of detected voids. Yellow marks correspond to voids detected using acoustic microscopy data. Red marks indicate where voids were confirmed by X-ray microscopy. White circles indicate where defect contacts were verified by cross-sectioning and SEM imaging. SEM investigations were only performed on column 3 and 4 (counted from the right-hand-side of the device). RIGHT: superimposed parameter maps. Red indication corresponds to pulse separation in the "void-range". Blue marks indicate the wavelet coefficients and green stains everything that is not detected as an interconnect.

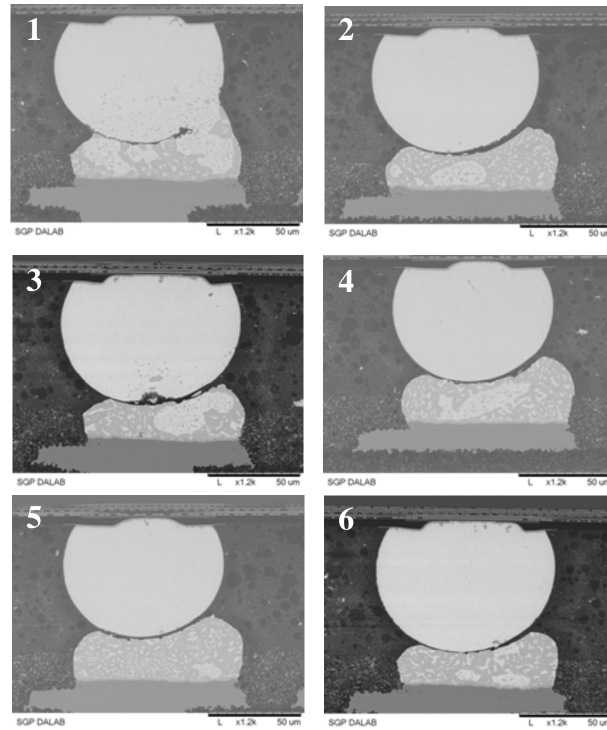

Figure 10: Scanning electron micrographs of defective flip-chip interconnects in the investigated CPU-device. The numbering corresponds to the numbering in Fig.9-center which shows the lateral positions of the contacts.

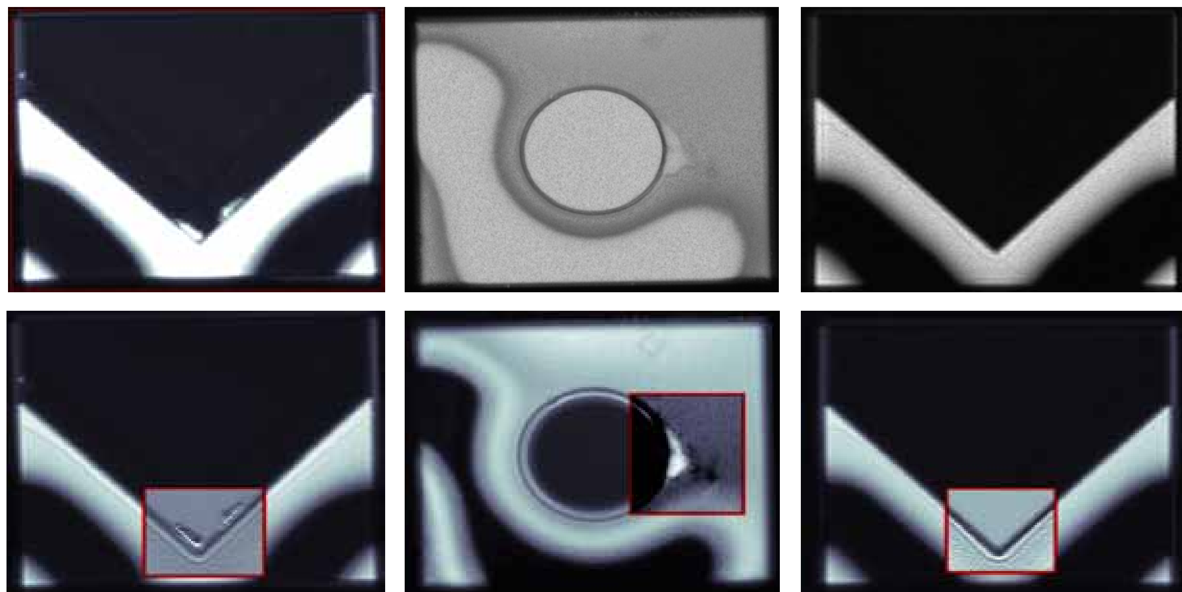

Figure 11: Image analysis applied to acoustic micrographs. Top: pure intensity images obtained by an acoustic microscope. Bottom: processed acoustic images. Image filters for blind-deconvolution and a Gaussian filter were applied to emphasize the defect and for increasing the resolution. A Sobel filter was applied in the lower left- and right images for detecting the contour and orientation of the defects.

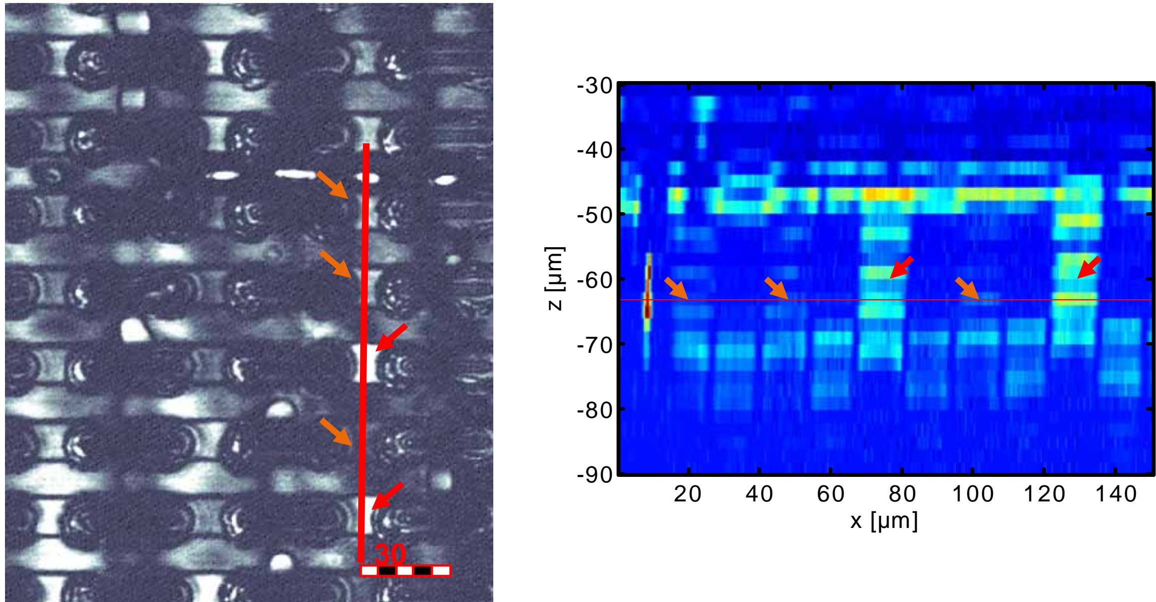

Figure 12: Acoustic GHz-Microscopy data acquisition at decreasing distances between acoustic lens and sample surface. Left: Acoustic micrograph recorded with sufficient defocus for imaging the electrical routings between the micro-bumps. This layer is buried behind 5 µm of BCB. Right: Acoustic cross-section along the red marked line in the acoustic micrograph (right). At approx. -45 µm the sample surface is in focus. The image displayed on the right was recorded at approx. -60 µm which corresponds to a defocus of 15 µm.

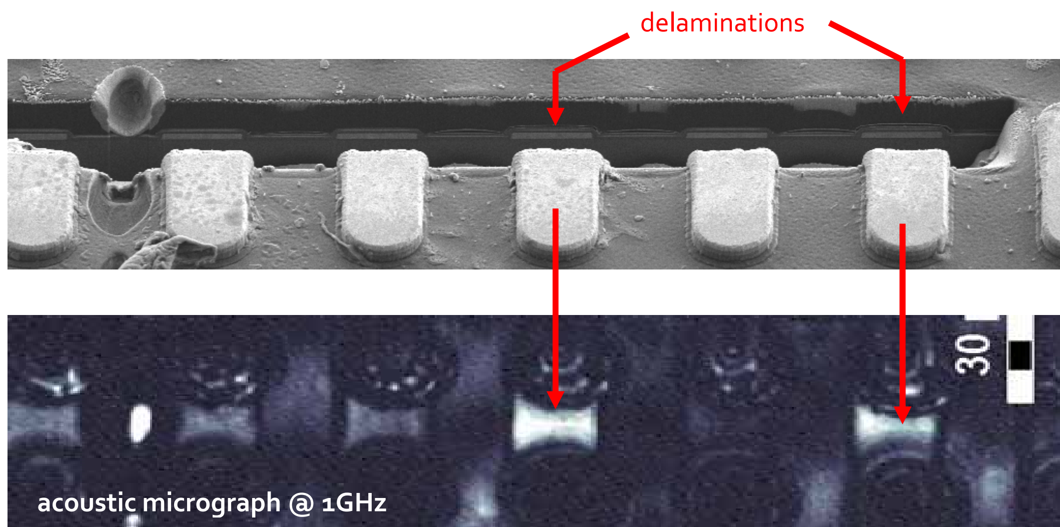

Figure 13: Acoustic GHz-Microscopy for localizing defects in the electrical routings. TOP: SEM image with a FIB created trench for micro cross-sectioning. Bottom acoustic micrograph recorded at 1 GHz with the acoustic focus placed inside the specimen. Delaminations (indicated by the arrows) appear bright in the acoustic micrograph.

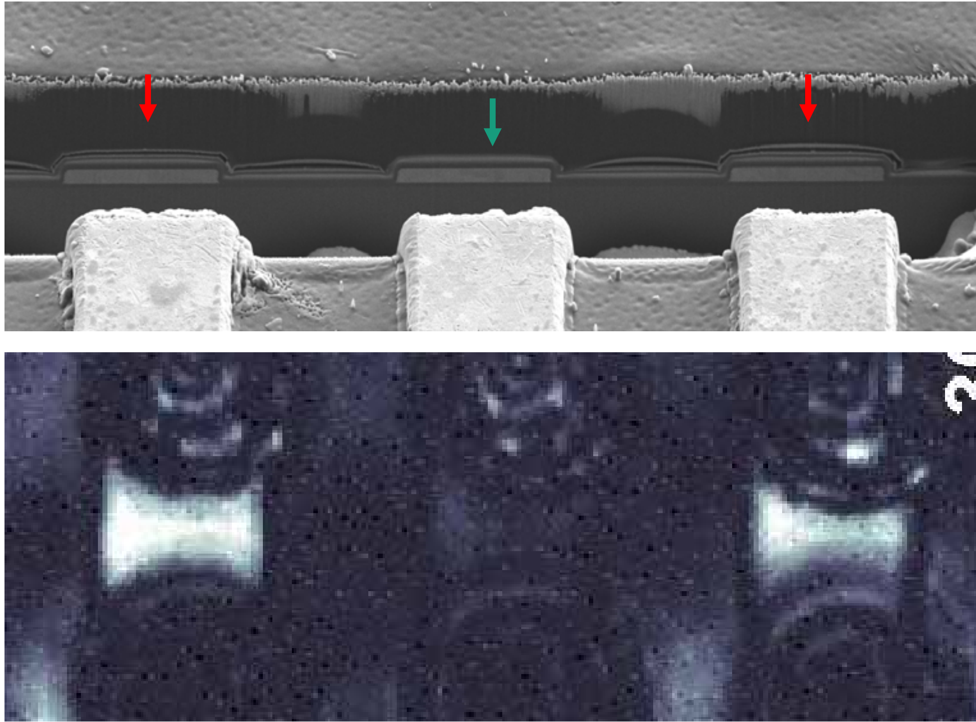

Figure 14: Acoustic GHz-microscopy at 1 Ghz with enlarged SEM image for displaying the detail of the delamination. TOP: SEM image of the FIB processed trench. Bottom corresponding acoustic micrograph. Delaminations are clearly visisble in the SEM image that confirms the findings of the acoustic microscopy.